

CCD Photometry, Light Curve Modeling, and Period Study of V573 Serpentis, a Totally Eclipsing Overcontact Binary System

Kevin B. Alton

Desert Blooms Observatory, 70 Summit Avenue, Cedar Knolls, NJ 07927; kbalton@optonline.net

Edward O. Wiley

Live Oaks Observatory, 125 Mountain Creek Pass, Georgetown, TX 78633; ewiley@suddenlink.net

Received June 18, 2021; revised July 21, 2021; accepted July 29, 2021

Abstract Precise time-series multi-color light curve data were acquired from V573 Ser at Desert Blooms Observatory (DBO) in 2019 and Live Oaks Observatory (LOO) in 2020. Previously, only monochromatic CCD-derived photometric data were available from automated surveys which employ sparse sampling strategies. New times-of-minimum from data acquired at DBO and LOO, along with other eclipse timings extrapolated from selected surveys, were used to generate a new linear ephemeris. Secular analyses (eclipse timing differences vs. epoch) did not reveal changes in the orbital period of V573 Ser over the past 20 years. Simultaneous modeling of multicolor light curve data during each epoch was accomplished using the Wilson-Devinney code. Since a total eclipse is observed, a unique photometrically derived value for the mass ratio (q_{pim}) could be determined, which subsequently provided initial estimates for the physical and geometric elements of each variable system.

1. Introduction

Overcontact binaries (OCBs), also known as EW or W UMA-type variables, share a common atmosphere with varying degrees of physical contact. Light curves (LCs) may exhibit eclipse minima with near equal depth that reveal little color change, suggesting they have similar surface temperatures. When the most massive constituent is defined as the primary star the majority of OCBs have mass ratios ($q = m_2/m_1$) that range from unity to as low as 0.065–0.08 (Sriram *et al.* 2016; Mochnacki and Doughty 1972; Paczyński *et al.* 2007; Arbutina 2009). The evolutionary lifetimes of most OCBs are spent in physical contact (Stepień 2006; Gazeas and Stepień 2008; Stepień and Kiraga 2015). Moreover, depending on many factors, including rate of angular momentum loss, mass ratio, total mass, orbital period, and metallicity, OCBs are destined to coalesce into fast rotating stars or to alternatively produce exotic objects such as blue stragglers (Qian *et al.* 2006; Stepień and Kiraga 2015), double degenerate binaries, supernovae, or even double black holes (Almeida *et al.* 2015).

Sparingly sampled monochromatic photometric data for V573 Ser (= NSVS 13459733) were first captured during the ROTSE-I survey between 1999 and 2000 (Akerlof *et al.* 2000; Woźniak *et al.* 2004; Gettel *et al.* 2006). These data can be retrieved from the Northern Sky Variable Survey (NSVS) archives. Other sources which include photometric data from this variable system are the All Sky Automated Survey (ASAS) (Pojmański *et al.* 2005), Catalina Sky Survey (Drake *et al.* 2014), and the All-Sky Automated Survey for SuperNovae (ASAS-SN) (Shappee *et al.* 2014; Kochanek *et al.* 2017; Jayasinghe *et al.* 2018).

No multi-color light curves with Roche modeling have been reported for this OCB so this investigation also provides the first published photometric mass ratio (q_{pim}) estimates along with preliminary physical and geometric characteristics for V573 Ser.

2. Observations and data reduction

Precise time-series images were acquired at Desert Blooms Observatory (DBO, USA; 31.941 N, 110.257 W) using a QSI 683 wsg-8 CCD camera mounted at the Cassegrain focus of a 0.4-m Schmidt-Cassegrain telescope. A Taurus 400 (Software Bisque) equatorial fork mount facilitated continuous operation without the need to perform a meridian flip. The image (science, darks, and flats) acquisition software (THE SKY X Pro Edition 10.50.0; Software Bisque 2019) controlled the main and integrated guide cameras. This focal-reduced ($f/7.2$) instrument produces an image scale of 0.76 arcsec/pixel ($\text{bin}=2 \times 2$) and a field-of-view (FOV) of 15.9×21.1 arcmin. Computer time was updated immediately prior to each session and exposure time for all images adjusted to 75 s.

The equipment at Live Oaks Observatory LOO, USA; 30.98 N, 98.94 W) included an Astrophysics AP900 GEM with a Moravian G2-1600 Mk.1 CCD camera mounted at the Cassegrain focus of a 0.28-m Schmidt-Cassegrain telescope. PDCAPTURE (Miller 2021) controlled the main and integrated guide cameras during image acquisition (science, darks, and flats). This focal-reduced ($f/7$) instrument produces an image scale of 0.95 arcsec/pixel ($\text{bin}=1 \times 1$) and a field-of-view (FOV) of 16×24 arcmin.

Both CCD cameras were equipped with Astrodon B, V, and I_c filters manufactured to match the Johnson-Cousins Bessell specification. Dark subtraction, flat correction, and registration of all images collected at DBO were performed with AIP4WIN v2.4.0 (Berry and Burnell 2005), whereas image calibration at LOO was accomplished with AstroImageJ (Collins *et al.* 2017). Instrumental readings from V573 Ser were reduced to catalog-based magnitudes using APASS DR9 values (Henden *et al.* 2009, 2010, 2011; Smith *et al.* 2011) built into MPO CANOPUS v10.7.1.3 (Minor Planet Observer 2010).

Table 1. Astrometric coordinates (J2000), V mags, and color indices (B–V) for V573 Ser (Figure 1), and the corresponding comparison stars used in this photometric study.

<i>Star Identification</i>	<i>R.A. (J2000)^a</i> <i>h m s</i>	<i>Dec. (J2000)^a</i> <i>° ' "</i>	<i>V mag^b</i>	<i>(B–V)^b</i>
(T) V573 Ser	15 59 29.7958	+02 52 21.157	12.846	0.844
(1) GSC 00357-0083	15 59 07.4064	+02 57 27.67	11.635	0.865
(2) GSC 00357-0889	15 59 32.7151	+03 02 03.797	12.368	0.836
(3) GSC 00357-0781	15 59 38.6095	+03 02 26.849	11.886	0.790
(4) GSC 00357-0081	15 59 26.1398	+02 57 19.442	13.276	0.726
(5) GSC 00357-0117	15 59 20.6231	+02 55 25.872	12.79	0.703

a. *R.A. and Dec. from Gaia DR2 (Gaia Collab. et al. 2016, 2018).*

b. *V-mag and (B–V) for comparison stars derived from APASS DR9 database described by Henden et al. (2009, 2010, 2011) and Smith et al. (2011).*

Table 2. Summary of image acquisition dates, number of data points and estimated uncertainty (\pm mag) in each bandpass (BVI_c) used for the determination of ToM values and/or Roche modeling.

<i>Target ID</i>	<i>B</i>	<i>B (\pm mag)</i>	<i>V</i>	<i>V (\pm mag)</i>	<i>I_c</i>	<i>I_c (\pm mag)</i>	<i>Location</i>	<i>Dates</i>
V573 Ser	264	0.008	267	0.004	266	0.005	DBO	June 19, 2019–June 25, 2019
V573 Ser	566	0.023	452	0.011	619	0.015	LOO	April 22, 2020–July 20, 2020

3. Results and discussion

Light curves were generated using an ensemble of five comparison stars, the mean of which remained constant (<0.01 mag) throughout each imaging session. The identity, J2000 coordinates, and color indices (B–V) for these stars are provided in Table 1. A CCD image annotated with the location of the target (T) and comparison stars (1–5) is shown in Figure 1. Only data acquired above 30° altitude (airmass <2.0) were included; differential atmospheric extinction was ignored, considering the close proximity of all program stars.

All photometric data can be retrieved from the AAVSO International Database via the International Variable Star Index (Kafka 2021).

3.1. Photometry and ephemerides

Times of minimum (ToM) and associated errors were calculated using the method of Kwee and van Woerden (1956) as implemented in PERANSO v2.5 (Paunzen and Vanmunster 2016). Curve fitting all eclipse timing differences (ETD) was accomplished using scaled Levenberg-Marquardt algorithms (QTIPLOT 0.9.9-rc9; IONDEV SRL 2021). Photometric uncertainty was calculated according to the so-called “CCD Equation” (Mortara and Fowler 1981; Howell 2006). The acquisition dates, number of data points, and uncertainty for each bandpass used for the determination of ToM values and/or Roche modeling are summarized in Table 2.

Thirteen new ToM measurements were extracted from photometric data acquired at DBO and LOO. These, along with seven other eclipse timings (Table 3), were used to calculate a new linear ephemeris (Figure 2) based on data produced between 1999 and 2020:

$$\text{Min.I(HJD)} = 2459046.5366 (5) + 0.3751703 (1)E. \quad (1)$$

Given the paucity of data, no other underlying variations in the orbital period stand out such as those that might be caused by angular momentum loss/gain, mass transfer, magnetic

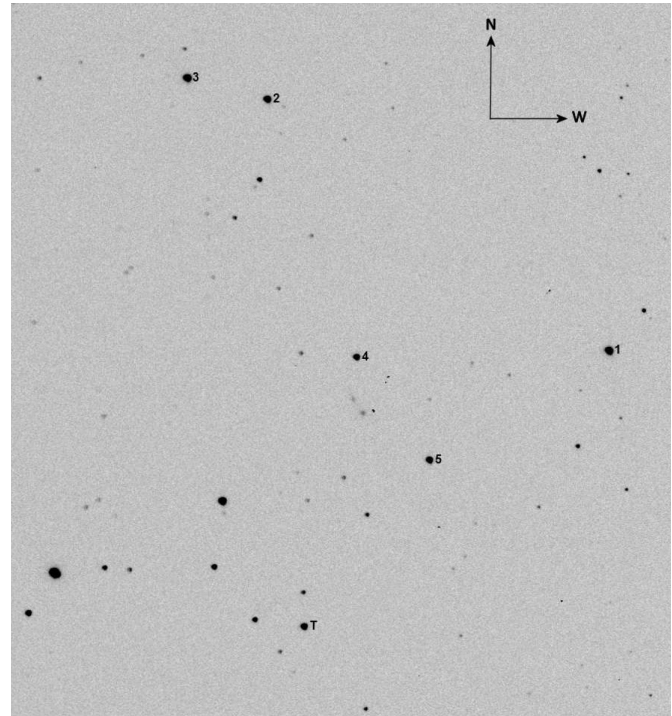


Figure 1. CCD image (V mag) of V573 Ser (T) acquired at DBO showing the location of comparison stars (1–5) used to generate APASS DR9-derived magnitude estimates.

cycles (Applegate 1992), or the presence of an additional gravitationally bound stellar-size body. At a minimum, another decade of precise times of minimum will still be needed to establish whether the orbital period of this system is changing in a predictable fashion.

3.2. Effective temperature estimation

The effective temperature (T_{eff}) of the more massive, and therefore most luminous component (defined as the primary star herein) was derived from a composite of astrometric (UCAC4; Zacharias *et al.* 2013) and photometric (2MASS

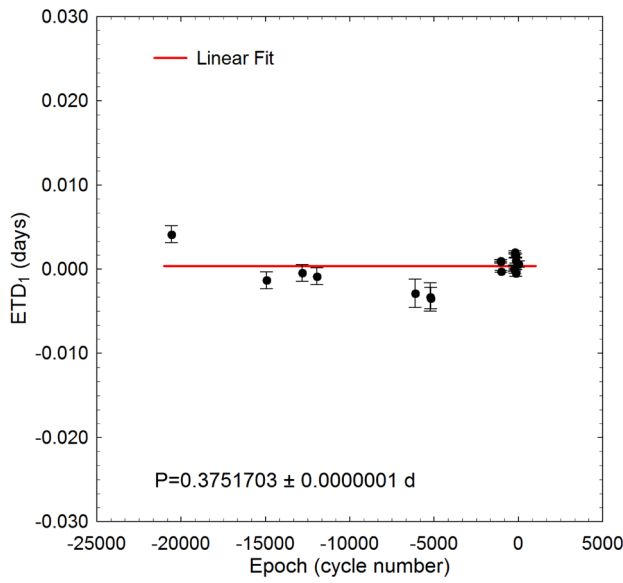


Figure 2. Eclipse timing differences (ETD) vs. epoch for V573 Ser calculated using the updated linear (Equation 1). When available, measurement uncertainty is denoted by the hatched error bars. The solid red line indicates the linear fit.

Table 3. V573 Ser times of minimum (February 23, 1999–July 16, 2020), cycle number and residuals (ETD) between observed and predicted times derived from the updated linear ephemeris (Equation 1).

HJD 2400000+	HJD Error	Cycle No.	ETD ^a	Reference
51321.7837	0.0010	−20590	0.004147	1
53438.8644	0.0010	−14947	−0.001309	1
54239.8539	0.0010	−12812	−0.000457	2
54564.9386	0.0010	−11945.5	−0.000845	2
56751.9920	0.0017	−6116	−0.002867	3
57084.0173	0.0017	−5231	−0.003306	3
57099.9619	0.0013	−5188.5	−0.003445	4
58655.7976	0.0002	−1041.5	0.000924	4
58657.6735	0.0001	−1036.5	0.000970	4
58659.7357	0.0001	−1031	−0.000253	4
58962.8737	0.0003	−223	0.000055	4
58963.8135	0.0002	−220.5	0.001981	4
58964.7493	0.0003	−218	−0.000183	4
58965.8751	0.0003	−215	0.000180	4
58966.8146	0.0003	−212.5	0.001659	4
58987.8234	0.0003	−156.5	0.001015	4
58989.6999	0.0002	−151.5	0.001610	4
58989.8854	0.0004	−151	−0.000465	4
59046.7248	0.0004	0.5	0.000591	4

a. ETD = Eclipse Time Difference.

References: 1. *NSVS* (Woźniak et al. 2004); 2. *CSS* (Univ. Arizona 2020); 3. *ASAS-SN* (Shappee et al. 2014; Kohanek et al. 2017); 4. *This study*.

and APASS; Skrutskie et al. 2006; Henden et al. 2016) determinations that were as necessary transformed to $(B-V)^{1,2}$. Interstellar extinction (A_V) and reddening ($E(B-V) = A_V / 3.1$) were estimated for targets within the Milky Way Galaxy according to Amôres and Lépine (2005). These models³ require the Galactic coordinates (l, b) and the distance in kpc (Bailer-Jones 2015). After subtracting out reddening to arrive at a value for intrinsic color, $(B-V)_0$, T_{eff1} estimates were interpolated for each system using the values reported for main sequence dwarf

Table 4. Estimation of effective temperature (T_{eff1}) of the primary star in V573 Ser.

Parameter	V573 Ser
Median combined $(B-V)_0^a$	0.802 ± 0.023
Galactic reddening $E(B-V)^b$	0.043 ± 0.001
Survey T_{eff1}^c (K)	5300 ± 86
Gaia T_{eff1}^d (K)	5313^{+540}_{-433}
Houdashelt T_{eff1}^e (K)	5356 ± 305
LAMOST DR5 T_{eff1}^f (K)	5492 ± 31
Median T_{eff1} (K)	5365 ± 220
Spectral Class	G6V ^g

a. Surveys and DBO intrinsic $(B-V)_0$ determined using reddening values ($E(B-V)$).

b. Model A (<http://www.galexin.org>).

c. T_{eff1} interpolated from median combined $(B-V)_0$ using Table 4 in Pecaut and Mamajek (2013).

d. Values from Gaia DR2 (Gaia Collab. 2016, 2018; <http://vizier.u-strasbg.fr/viz-bin/VizieR?-source=1/345/gaia2>).

e. Values calculated with Houdashelt et al. (2000) empirical relationship.

f. Values from LAMOST DR5 v3 (Natnl. Astron. Obs. Chinese Acad. Sci. 2005–2019; <http://dr5.lamost.org/search>).

g. Spectral class from LAMOST DR5.

stars by Pecaut and Mamajek (2013). Additional sources used to establish a median value for each T_{eff1} included low resolution spectra obtained from LAMOST-DR5 (Zhao et al. 2012; Wang et al. 2019), the Gaia DR2 release of stellar parameters (Andrae et al. 2018), and an empirical relationship (Houdashelt et al. 2000) based on intrinsic color where $0.32 \leq (B-V)_0 \leq 1.35$. The median result ($T_{\text{eff1}} = 5365 \pm 220$ K), summarized in Table 4, was adopted for Roche modeling of LCs from V573 Ser.

3.3. Roche modeling approach

Roche modeling of LC data during each epoch (2019 and 2020) was initially performed with PHOEBE 0.31a (Prša and Zwitter 2005) and then refined using WDWINT56A (Nelson 2009). Both programs feature a MS Windows-compatible GUI interface to the Wilson-Devinney WD2003 code (Wilson and Devinney 1971; Wilson 1979; Wilson 1990). WDWINT56A incorporates Kurucz's atmosphere models (Kurucz 2002) that are integrated over BVI_c passbands. The final selected model was Mode 3 for an overcontact binary; other modes (detached and semi-detached) never approached the best fit value (χ^2) achieved with Mode 3 using PHOEBE 0.31a. Modeling parameters were adjusted as follows. The internal energy transfer to the stellar surface is driven by convective (7500 K) rather than radiative processes. As a result, the value for bolometric albedo ($A_{1,2} = 0.5$) was assigned according to Ruciński (1969) while the gravity darkening coefficient ($g_{1,2} = 0.32$) was adopted from Lucy (1967). Logarithmic limb darkening coefficients (x_1, x_2, y_1, y_2) were interpolated (van Hamme 1993) following any change in the effective temperature (T_{eff2}) of the secondary star during model fit optimization using differential corrections (DC). All but the temperature of the more massive star (T_{eff1}), $A_{1,2}$, and $g_{1,2}$ were allowed to vary during DC iterations. In general, the best fits for T_{eff2} , i , q , and Roche potentials ($\Omega_1 = \Omega_2$) were collectively refined (method of multiple subsets) by DC using

1. http://www.aerith.net/astro/color_conversion.html. 2. <http://brucegary.net/dummies/method0.html>. 3. <http://www.galexin.org>.

the multicolor LC data until a simultaneous solution was found. Not uncommon for OCB systems, LCs from V573 Ser exhibit varying degrees of asymmetry during quadrature (Max I > Max II), which is often called the O'Connell effect (O'Connell 1951). Surface inhomogeneity often attributed to star spots was simulated by the addition of a hot and cool spot on the primary star to obtain the best fit LC models. V573 Ser did not require third light correction ($l_3 = 0$) to improve Roche model fits.

3.4. Roche modeling results

Without radial velocity (RV) data it is generally not possible to unambiguously determine the mass ratio, subtype (A or W), or total mass of an eclipsing binary system. Nonetheless, since a total eclipse is observed, a unique mass ratio value could be found (Terrell and Wilson 2005). Standard errors reported in Tables 5 and 6 are computed from the DC covariance matrix and only reflect the model fit to the observations which assume exact values for any fixed parameter. These errors are generally regarded as unrealistically small considering the estimated uncertainties associated with the mean adopted T_{eff1} values along with basic assumptions about $A_{1,2}$, $g_{1,2}$, and the influence of spots added to the Roche model. Normally, the value for T_{eff1} is fixed with no error during modeling with the W-D code

Table 5. Lightcurve parameters evaluated by Roche modeling and the geometric elements derived for V573 Ser (2019) assuming it is a W-type W UMa variable.

Parameter ^a	DBO	DBO
	No Spot	Spotted
T_{eff1} (K) ^b	5365	5365
T_{eff2} (K)	5728 (3)	5672 (14)
q (m_2/m_1)	0.367 (1)	0.373 (3)
A^b	0.50	0.50
g^b	0.32	0.32
$\Omega_1 = \Omega_2$	2.573 (2)	2.583 (4)
i°	89.7 (4)	83.9 (4)
$A_p = T_s/T_{\text{star}}^c$	—	1.10 (1)
θ_p (spot co-latitude) ^c	—	90 (4)
ϕ_p (spot longitude) ^c	—	75 (3)
r_p (angular radius) ^c	—	10.2 (1)
$A_p = T_p/T_{\text{star}}^c$	—	0.86 (1)
θ_p (spot co-latitude) ^c	—	90 (2)
ϕ_p (spot longitude) ^c	—	180 (2)
ϕ_p (spot longitude) ^c	—	11.3 (1)
$L_1/(L_1+L_2)B^d$	0.6197 (4)	0.6307 (4)
$L_1/(L_1+L_2)V$	0.6441 (2)	0.6512 (1)
$L_1/(L_1+L_2)I_c$	0.6634 (2)	0.6676 (2)
r_1 (pole)	0.4472 (3)	0.4459 (6)
r_1 (side)	0.4802 (4)	0.4785 (7)
r_1 (back)	0.5094 (6)	0.5076 (8)
r_2 (pole)	0.2848 (4)	0.2850 (15)
r_2 (side)	0.2980 (4)	0.2981 (18)
r_2 (back)	0.3371 (7)	0.3367 (33)
Fill-out factor (%)	16.8	16.9
RMS (B) ^e	0.01398	0.01189
RMS (V)	0.00880	0.00614
RMS (I _c)	0.01063	0.00843

a. All uncertainty estimates for T_{eff2} , q , $\Omega_{1,2}$, i , $r_{1,2}$ and L_1 from *WDWINT56A* (Nelson 2009).

b. Fixed with no error during DC.

c. Spot parameters in degrees (θ_p , ϕ_p , and r_p) or A_p in fractional degrees (K).

d. L_1 and L_2 refer to scaled luminosities of the primary and secondary stars, respectively.

e. Monochromatic residual mean square error from observed values.

despite measurement uncertainty which can approach 10% relative standard deviation (R.S.D.) without supporting high resolution spectral data. The effect that such uncertainty in T_{eff1} would have on modeling estimates for q , i , $\Omega_{1,2}$, and T_{eff2} has been investigated with other OCBs including A- (Alton 2019; Alton *et al.* 2020) and W-subtypes (Alton and Nelson 2018). As might be expected, any change in the fixed value for T_{eff1} results in a corresponding change in the T_{eff2} . These findings are consistent whereby the uncertainty in the model fit for T_{eff2} would be essentially the same as that established for T_{eff1} . Furthermore, varying T_{eff1} by as much as 10% did not appreciably affect the uncertainty estimates (R.S.D. < 2.2%) for i , q , or $\Omega_{1,2}$ (Alton 2019; Alton and Nelson 2018; Alton *et al.* 2020). Assuming that the actual T_{eff1} value falls within 10% of the adopted values used for Roche modeling (a reasonable expectation based on T_{eff1} data provided in Table 4), then uncertainty estimates for i , q , or $\Omega_{1,2}$, along with spot size, temperature, and location, would likely not exceed 2.2% R.S.D.

The fill-out parameter (f) which corresponds to the outer surface shared by each star was calculated according to Equation 2 (Kallrath and Malone 2009; Bradstreet 2005) where:

$$f = (\Omega_{\text{inner}} - \Omega_{1,2}) / (\Omega_{\text{inner}} - \Omega_{\text{outer}}), \quad (2)$$

Table 6. Lightcurve parameters evaluated by Roche modeling and the geometric elements derived for V573 Ser (2020) assuming it is a W-type W UMa variable.

Parameter ^a	LOO	LOO
	No Spot	Spotted
T_{eff1} (K) ^b	5365	5365
T_{eff2} (K)	5649 (2)	5581 (1)
q (m_2/m_1)	0.369 (1)	0.381 (1)
A^b	0.50	0.50
g^b	0.32	0.32
$\Omega_1 = \Omega_2$	2.577 (2)	2.592 (3)
i°	86.12 (4)	83.8 (3)
$A_p = T_s/T_{\text{star}}^c$	—	1.09(1)
θ_p (spot co-latitude) ^c	—	90 (2)
ϕ_p (spot longitude) ^c	—	60 (4)
r_p (angular radius) ^c	—	10.6 (2)
$A_p = T_p/T_{\text{star}}^c$	—	0.90 (1)
θ_p (spot co-latitude) ^c	—	90 (3)
ϕ_p (spot longitude) ^c	—	180 (2)
ϕ_p (spot longitude) ^c	—	11 (2)
$L_1/(L_1+L_2)B^d$	0.6383 (3)	0.6360 (3)
$L_1/(L_1+L_2)V$	0.6573 (2)	0.6574 (2)
$L_1/(L_1+L_2)I_c$	0.6724 (2)	0.6743 (2)
r_1 (pole)	0.4469 (4)	0.4456 (5)
r_1 (side)	0.4798 (5)	0.4783 (6)
r_1 (back)	0.5092 (6)	0.5082 (7)
r_2 (pole)	0.2855 (4)	0.2882 (11)
r_2 (side)	0.2988 (5)	0.3018 (14)
r_2 (back)	0.3381 (8)	0.3416 (26)
Fill-out factor (%)	16.8	20.0
RMS (B) ^e	0.01261	0.01101
RMS (V)	0.00766	0.00633
RMS (I _c)	0.00970	0.00983

a. All uncertainty estimates for T_{eff2} , q , $\Omega_{1,2}$, i , $r_{1,2}$ and L_1 from *WDWINT56A* (Nelson 2009).

b. Fixed with no error during DC.

c. Spot parameters in degrees (θ_p , ϕ_p , and r_p) or A_p in fractional degrees (K).

d. L_1 and L_2 refer to scaled luminosities of the primary and secondary stars, respectively.

e. Monochromatic residual mean square error from observed values.

wherein Ω_{outer} is the outer critical Roche equipotential, Ω_{inner} is the value for the inner critical Roche equipotential, and $\Omega = \Omega_{1,2}$ denotes the common envelope surface potential for the binary system. In all cases the systems are considered overcontact since $0 < f < 1$.

LC parameters, geometric elements, and their corresponding uncertainties are summarized in Tables 5 (2019) and 6 (2020). According to Binnendijk (1970) the deepest minimum (Min I) of a W-type overcontact system occurs when a cooler more massive constituent occludes its hotter but less massive binary partner. The flattened-bottom dip in brightness at Min I (Figures 3 and 4) indicates a total eclipse of the secondary star;

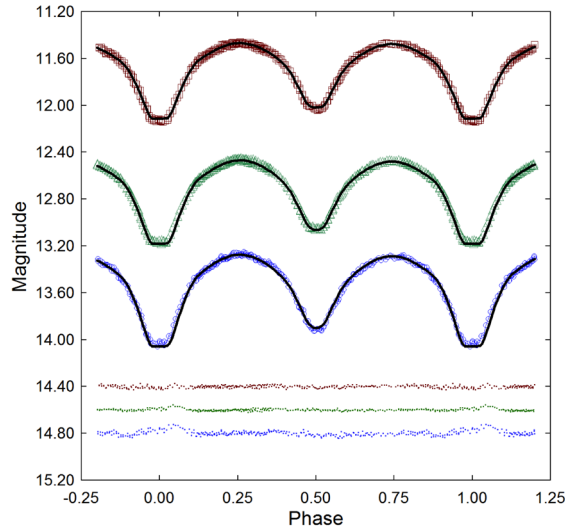


Figure 3. Period folded (0.3751703 ± 0.0000001 d) CCD-derived LCs for V573 Ser produced from photometric data collected at DBO between June 19, 2019 and June 25, 2019. The top (I_V), middle (V) and bottom curve (B) were transformed to magnitudes based on APASS DR9 derived catalog values from comparison stars. In this case, the Roche model assumed a W-subtype overcontact binary with two spots on the most massive star; residuals from the model fits are offset at the bottom of the plot to keep the values on scale.

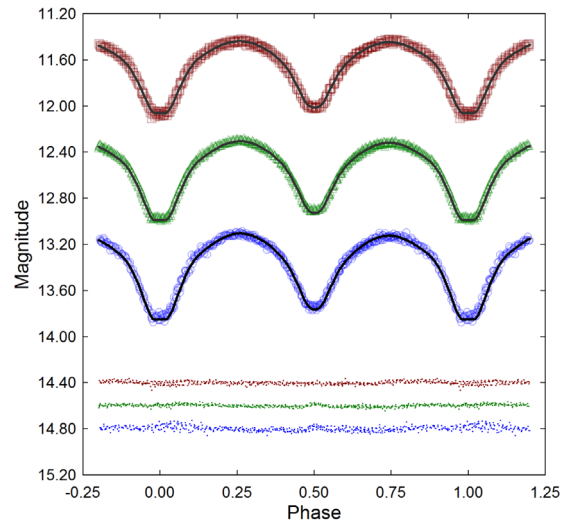


Figure 4. Period folded (0.3751703 ± 0.0000001 d) CCD lightcurves acquired from V573 Ser at LOO between April 22, 2020 and July 20, 2020. The remaining caption is the same as Figure 3.

Table 7. Fundamental stellar parameters for V573 Ser using the mean photometric mass ratio ($q_{\text{ptm}} = m_2/m_1$) from Roche model fits of LC data (2019–2020) and the estimated masses based on empirically derived M-PRs for overcontact binary systems.

Parameter	Primary	Secondary
Mass (M_{\odot})	1.230 ± 0.023	0.446 ± 0.009
Radius (R_{\odot})	1.218 ± 0.006	0.768 ± 0.004
a (R_{\odot})	2.600 ± 0.013	2.600 ± 0.013
Luminosity (L_{\odot})	1.108 ± 0.257	0.557 ± 0.006
M_{bol}	4.639 ± 0.011	5.385 ± 0.012
Log (g)	4.356 ± 0.009	4.316 ± 0.009

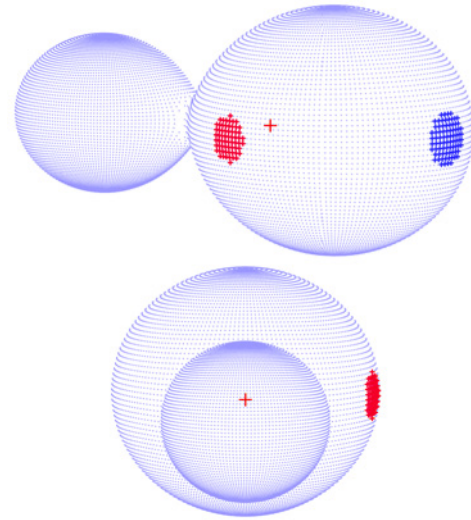


Figure 5. Three-dimensional spatial model of V573 Ser during 2019 illustrating (top) the location of a cool (blue) and hot (red) spot on the primary star and (bottom) the secondary star transit across the primary star face at Min II ($\phi = 0.5$).

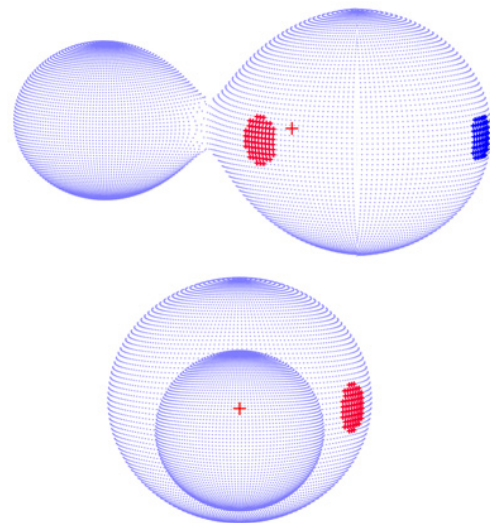


Figure 6. Three-dimensional spatial model of V573 Ser during 2020 illustrating (top) the location of a hot (red) and cool (blue) spot on the primary star and (bottom) the secondary star transit across the primary star face at Min II ($\phi = 0.5$).

therefore, W-D modeling proceeded under the assumption that V573 Ser is a W-subtype. Since according to the convention used herein whereby the primary star is the most massive ($m_2/m_1 \leq 1$), a phase shift (0.5) was introduced to properly align the LC for subsequent Roche modeling. Even though photometric data were acquired between 2019 and 2020 using different instruments at two sites, the modeled results for V573 Ser compare quite favorably. It would also appear that the surface inhomogeneity modeled with hot and cool spots on the primary star was similar and persisted between June 19, 2019, and July 20, 2020.

Spatial renderings (Figures 5 and 6) were produced with BINARYMAKER3 (BM3: Bradstreet and Steelman 2004) using the final WDWINT56A modeling results from both epochs (2019 and 2020). A secondary star can be envisioned to completely transit across the primary face during Min II ($\phi=0.5$), thereby confirming that the secondary star is totally eclipsed at Min I.

3.5. Preliminary stellar parameters

Mean physical characteristics were estimated for V573 Ser (Table 7) using results from the best fit (spotted) LC simulations from 2019 and 2020. It is important to note that without the benefit of RV data which define the orbital motion, mass ratio, and total mass of the binary pair, these results should be considered “relative” rather than “absolute” parameters and regarded as preliminary.

Calculations are described below for estimating the solar mass and size, semi-major axis, solar luminosity, bolometric V-mag, and surface gravity of each component. Three empirically-derived mass-period relationships (M-PR) for W UMa binaries have been published. The first M-PR was reported by Qian (2003), while two others followed from Gazeas and Stepień (2008) and then Gazeas (2009). According to Qian (2003), when the primary star is less than $1.35 M_\odot$ or the system is W-type its mass can be determined from Equation 3:

$$\log(M_1) = 0.391 (59) \cdot \log(P) + 1.96 (17), \quad (3)$$

where P is the orbital period in days and leads to $M_1 = 1.126 \pm 0.087 M_\odot$ for the primary. The M-PR (Equation 4) derived by Gazeas and Stepień (2008):

$$\log(M_1) = 0.755 (59) \cdot \log(P) + 0.416 (24), \quad (4)$$

corresponds to an OCB system where $M_1 = 1.243 \pm 0.099 M_\odot$. Gazeas (2009) reported another empirical relationship (Equation 5) for the more massive (M_1) star of a contact binary such that:

$$\log(M_1) = 0.725 (59) \cdot \log(P) - 0.076 (32) \cdot \log(q) + 0.365 (32). \quad (5)$$

from which $M_1 = 1.228 \pm 0.091 M_\odot$. The mean of three values ($M_1 = 1.230 \pm 0.023 M_\odot$) estimated from Equations 3–5 was used for subsequent determinations of M_2 , semi-major axis a, volume radii r_L , and bolometric magnitudes (M_{bol}) using the formal errors calculated by WDWINT56A (Nelson 2009). The secondary mass = $0.446 \pm 0.009 M_\odot$ and total mass ($1.676 \pm 0.025 M_\odot$)

were determined using the mean photometric mass ratio ($q_{\text{ptm}} = 0.377 \pm 0.006$) derived from the best fit (spotted) models.

The semi-major axis, $a(R_\odot) = 2.600 \pm 0.013$, was calculated from Newton’s version (Equation 6) of Kepler’s third law where:

$$a^3 = (G \cdot P^2 (M_1 + M_2)) / (4\pi^2). \quad (6)$$

The effective radius of each Roche lobe (r_L) can be calculated over the entire range of mass ratios ($0 < q < \infty$) according to an expression (Equation 7) derived by Eggleton (1983):

$$r_L = (0.49q^{2/3}) / (0.6q^{2/3} + \ln(1 + q^{1/3})), \quad (7)$$

from which values for r_1 (0.4671 ± 0.0002) and r_2 (0.2967 ± 0.0002) were determined for the primary and secondary stars, respectively. Since the semi-major axis and the volume radii are known, the radii in solar units for both binary components can be calculated where $R_1 = a \cdot r_1 = 1.218 \pm 0.006 R_\odot$ and $R_2 = a \cdot r_2 = 0.768 \pm 0.004 R_\odot$.

Luminosity in solar units (L_\odot) for the primary (L_1) and secondary stars (L_2) was calculated from the well-known relationship derived from the Stefan-Boltzmann law (Equation 8) where:

$$L_{1,2} = (R_{1,2} / R_\odot)^2 (T_{1,2} / T_\odot)^4. \quad (8)$$

Assuming that $T_{\text{eff1}} = 5365 \text{ K}$, $T_{\text{eff2}} = 5690 \text{ K}$ and $T_\odot = 5772 \text{ K}$, then the solar luminosities (L_\odot) for the primary and secondary are $L_1 = 1.108 \pm 0.257$ and $L_2 = 0.557 \pm 0.006$, respectively. The Gaia DR2 reported values for radius ($1.026_{-0.021}^{+0.022}$) and luminosity ($1.2_{-0.23}^{+0.23}$) compare very favorably with our estimates for this binary system.

4. Conclusions

New times of minimum for V573 Ser ($n=13$) based on multicolor CCD data were determined from LCs acquired at two different locations in 2019 and 2020. These, along with other values extrapolated from multiple sparsely sampled monochromatic surveys, led to a linear ephemeris which suggests that the orbital period for this OCB has not changed significantly over the past 20 years.

The adopted effective temperature ($T_{\text{eff1}} = 5365 \pm 220 \text{ K}$) was based on a composite of sources that included values from photometric and astrometric surveys, the Gaia DR2 release of stellar characteristics (Andrae *et al.* 2018), and estimates from LAMOST DR5 spectral data (Zhao *et al.* 2012; Wang *et al.* 2019). V573 Ser clearly experiences a total eclipse which is evident as a flattened bottom during Min I, a characteristic of W-subtype variables. It follows that photometric mass ratios determined by Roche modeling should prove to be reliable substitutes for mass ratios derived from RV data. Nonetheless, spectroscopic studies (RV and high resolution classification spectra) will be required to unequivocally determine a total mass and spectral class for each system. Consequently, all parameter values and corresponding uncertainties reported herein should be considered preliminary.

5. Acknowledgements

This research has made use of the SIMBAD database operated at Centre de Données astronomiques de Strasbourg, France. In addition, the Northern Sky Variability Survey hosted by the Los Alamos National Laboratory (<https://skydot.lanl.gov/nsvs/nsvs.php>), the All Sky Automated Survey Catalogue of Variable Stars (<http://www.astrow.edu.pl/asas/?page=acvs>), All-Sky Automated Survey for Supernovae (<https://asas-sn.osu.edu/variables>), and the International Variable Star Index (AAVSO) were mined for essential information. This work also presents results from the European Space Agency (ESA) space mission Gaia. Gaia data are being processed by the Gaia Data Processing and Analysis Consortium (DPAC). Funding for the DPAC is provided by national institutions, in particular the institutions participating in the Gaia Multilateral Agreement (MLA). The Gaia mission website is <https://www.cosmos.esa.int/gaia>. The Gaia archive website is <https://archives.esac.esa.int/gaia>. This paper makes use of data from the first public release of the WASP data as provided by the WASP consortium and services at the NASA Exoplanet Archive, which is operated by the California Institute of Technology, under contract with the National Aeronautics and Space Administration under the Exoplanet Exploration Program. The use of public data from LAMOST is also acknowledged. Guoshoujing Telescope (the Large Sky Area Multi-Object Fiber Spectroscopic Telescope LAMOST) is a National Major Scientific Project built by the Chinese Academy of Sciences. Funding for the project has been provided by the National Development and Reform Commission. LAMOST is operated and managed by the National Astronomical Observatories, Chinese Academy of Sciences. Many thanks to the anonymous referee whose valuable commentary led to significant improvement of this paper.

References

- Akerlof, C., *et al.* 2000, *Astron. J.*, **119**, 1901.
 Almeida, L. A., *et al.* 2015, *Astrophys. J.*, **812**, 102.
 Alton, K. B. 2019, *J. Amer. Assoc. Var. Star Obs.*, **47**, 7.
 Alton, K. B., and Nelson, R. H. 2018, *Mon. Not. Roy. Astron. Soc.*, **479**, 3197.
 Alton, K. B., Nelson, R. H., and Stepień, K. 2020, *J. Astrophys. Astron.*, **41**, 26.
 Amôres, E. B., and Lépine, J. R. D. 2005, *Astron. J.*, **130**, 659.
 Andrae, R., *et al.* 2018, *Astron. Astrophys.*, **616A**, 8.
 Applegate, J. H. 1992, *Astrophys. J.*, **385**, 621.
 Arbutina, B. 2009, *Mon. Not. Roy. Astron. Soc.*, **394**, 501.
 Bailer-Jones, C. A. L. 2015, *Publ. Astron. Soc. Pacific*, **127**, 994.
 Berry, R., and Burnell, J. 2005, *The Handbook of Astronomical Image Processing*, 2nd ed., Willmann-Bell, Richmond, VA.
 Binnendijk, L. 1970, *Vistas Astron.*, **12**, 217.
 Bradstreet, D. H. 2005, in *The Society for Astronomical Sciences 24th Annual Symposium on Telescope Science*, Society for Astronomical Sciences, Rancho Cucamonga, CA, 23.
 Bradstreet, D. H., and Steelman, D. P. 2004, BINARY MAKER 3, Contact Software (<http://www.binarymaker.com>).
 Collins, K. A., Kielkopf, J. F., Stassun, K. G., and Hessman, F. V. 2017, *Astron. J.*, **153**, 77
 (<https://www.astro.louisville.edu/software/astroimagej>).
 Drake, A. J., *et al.* 2014, *Astrophys. J., Suppl. Ser.*, 213, 9.
 Eggleton, P. P. 1983, *Astrophys. J.*, **268**, 368.
 Gaia Collaboration, *et al.* 2016, *Astron. Astrophys.*, **595A**, 1.
 Gaia Collaboration, *et al.* 2018, *Astron. Astrophys.*, **616A**, 1.
 Gazeas, K. D. 2009, *Commun. Asteroseismology*, **159**, 129.
 Gazeas, K., and Stepień, K. 2008, *Mon. Not. Roy. Astron. Soc.*, **390**, 1577.
 Gettel, S. J., Geske, M. T., and McKay, T. A. 2006, *Astron. J.*, **131**, 621.
 Henden, A. A., Levine, S. E., Terrell, D., Smith, T. C., and Welch, D. L. 2011, *Bull. Amer. Astron. Soc.*, **43**, 2011.
 Henden, A. A., Terrell, D., Welch, D., and Smith, T. C. 2010, *Bull. Amer. Astron. Soc.*, **42**, 515.
 Henden, A. A., Welch, D. L., Terrell, D., and Levine, S. E. 2009, *Bull. Amer. Astron. Soc.*, **41**, 669.
 Henden, A. A., *et al.* 2015, AAVSO Photometric All-Sky Survey, data release 9 (<https://www.aavso.org/apass>).
 Houdashelt, M. L., Bell, R. A., and Sweigart, A. V. 2000, *Astron. J.*, **119**, 1448.
 Howell, S. B. 2006, *Handbook of CCD Astronomy*, 2nd ed., Cambridge Univ. Press, Cambridge, UK.
 IONDEV SRL. 2021, QTIPLLOT Data Analysis and Scientific Visualisation (<https://www.qtiplot.com/index.html>).
 Jayasinghe, T., *et al.* 2018, *Mon. Not. Roy. Astron. Soc.*, **477**, 3145.
 Kafka, S. 2021, Observations from the AAVSO International Database (<https://www.aavso.org/data-download>).
 Kallrath, J., and Milone, E. F. 2009, *Eclipsing Binary Stars: Modeling and Analysis*, Springer-Verlag, New York.
 Kochanek, C. S., *et al.* 2017, *Publ. Astron. Soc. Pacific*, **129**, 104502.
 Kurucz, R. L. 2002, *Baltic Astron.*, **11**, 101.
 Kwee, K. K., and van Woerden, H. 1956, *Bull. Astron. Inst. Netherlands*, **12**, 327.
 Lucy, L. B. 1967, *Z. Astrophys.*, **65**, 89.
 Miller, C. 2021, PDCAPTURE, version 2.1
 (<https://groups.io/g/pdcaptureapp>).
 Minor Planet Observer. 2010, MPO Software Suite (<http://www.minorplanetobserver.com>), BDW Publishing, Colorado Springs.
 Mochnacki, S. W., and Doughty, N. A. 1972, *Mon. Not. Roy. Astron. Soc.*, **156**, 51.
 Mortara, L., and Fowler, A. 1981, in *Solid State Imagers for Astronomy*, SPIE Conf. Proc. 290, Society for Photo-Optical Instrumentation Engineers, Bellingham, WA, 28.
 National Astronomical Observatories, Chinese Academy of Sciences. 2005–2019, Large Sky Area Multi-Object Fiber Spectroscopic Telescope (LAMOST) Data Release 5 v3 (<http://dr5.lamost.org>).
 Nelson, R. H. 2009, WDWINT56A: Astronomy Software by Bob Nelson (<https://www.variablestarssouth.org/bob-nelson>).
 O’Connell, D. J. K. 1951, *Publ. Riverview Coll. Obs.*, **2**, 85.
 Paunzen, E., and Vanmunster, T. 2016, *Astron. Nachr.*, **337**, 239.
 Pecaut, M., and Mamajek, E. E. 2013, *Astrophys. J., Suppl. Ser.*, **208**, 9.

- Paczynski, B., Sienkiewicz, R., and Szczygiel, D. M. 2007, *Mon. Not. Roy. Astron. Soc.*, **378**, 961.
- Pojmański, G., Pilecki, B., and Szczygiel, D. 2005, *Acta Astron.*, **55**, 275.
- Prša, A., and Zwitter, T. 2005, *Astrophys. J.*, **628**, 426.
- Qian, S. 2003, *Mon. Not. Roy. Astron. Soc.*, **342**, 1260.
- Qian, S., Yang, Y., Zhu, L., H., He, J., and Yuan, J. 2006, *Astrophys. Space Sci.*, **304**, 25.
- Ruciński, S. M. 1969, *Acta Astron.*, **19**, 245.
- Shappee, B. J., *et al.* 2014, *Astrophys. J.*, **788**, 48.
- Skrutskie, M. F., *et al.* 2006, *Astron. J.*, **131**, 1163.
- Smith, T. C., Henden, A. A., and Starkey, D. R. 2011, in *The Society for Astronomical Sciences 30th Annual Symposium on Telescope Science*, Society for Astronomical Sciences, Rancho Cucamonga, CA, 121.
- Software Bisque. 2019, THE SKYX professional edition 10.5.0 (<https://www.bisque.com>).
- Sriram, K., Malu, S., Choi, C.S., and Vivekananda Rao, P. 2016, *Astron. J.*, **151**, 69.
- Stepień, K. 2006, *Acta Astron.*, **56**, 199.
- Stepień, K., and Kiraga, M. 2015, *Astron. Astrophys.*, **577A**, 117.
- Terrell, D., and Wilson, R. E. 2005, *Astrophys. Space Sci.*, **296**, 221.
- University of Arizona. 2020, Catalina Sky Survey (<http://www.lpl.arizona.edu/css>).
- van Hamme, W. 1993, *Astron. J.*, **106**, 2096.
- Wang, R., *et al.* 2019, *Pub. Astron. Soc. Pacific*, **131**, 024505
- Wilson, R. E. 1979, *Astrophys. J.*, **234**, 1054.
- Wilson, R. E. 1990, *Astrophys. J.*, **356**, 613.
- Wilson, R. E., and Devinney, E. J., 1971, *Astrophys. J.*, **166**, 605.
- Woźniak, P. R., *et al.* 2004, *Astron. J.*, **127**, 2436.
- Zacharias, N., Finch, C. T., Girard, T. M., Henden, A., Bartlett, J. L., Monet, D. G., and Zacharias, M. I. 2013, *Astron. J.*, **145**, 44.
- Zhao, G., Zhao, Y.-H., Chu, Y.-Q., Jing, Y.-P., and Deng, L.-C. 2012, *Res. Astron. Astrophys.*, **12**, 723.